CrystEngComm

COMMUNICATION

View Article Online
View Journal | View Issue

Cite this: *CrystEngComm*, 2017, **19**, 4175

Received 23rd March 2017,
Accepted 19th May 2017

DOI: 10.1039/c7ce00552k

rsc.li/crystengcomm

Solution-based sequential modification of $LiCoO_2$ particle surfaces with iron(II) oxalate nanolayers†

Yuki Kishimoto,[a] So Yubuchi,[b] Akitoshi Hayashi,[b] Masahiro Tatsumisago[b] and Rie Makiura*[a]

Hybridization of metal–organic frameworks (MOFs) with other inorganic materials offers the opportunity to enhance their properties or open new windows for potential applications. Formation of core/shell structures, in which the core is the inorganic particle and the shell is the surface-deposited MOF, is one of the rational methodologies to create such hybrid materials. Here, we present the facile creation of metal oxide-core/MOF-shell structures by applying a solution-based step-by-step modification of the core surface using a framework compound. The modification procedure includes alternate immersion of $LiCoO_2$ (LCO) – a catalyst for the oxygen evolution reaction – into oxalic acid and ferrous solutions, resulting in the formation of iron(II) oxalate (Fe(ox), ox = oxalate anion) – one of the simplest MOFs with short unit frameworks – nanolayers on the LCO surface (Fe(ox)NL@LCO). The amount of deposited Fe(ox) does not increase monotonically with the number of the modification cycles, but tends to saturate rapidly, implying that the Fe(ox) framework grows laterally on the LCO surface. An increase of the electrical resistivity of the LCO particles that influences adversely catalytic activity is suppressed when a high coverage of the LCO surface by the Fe(ox) framework is achieved at subsequent modification cycles.

Crystalline coordination network materials with highly-regulated nanopores, the so-called metal–organic frameworks (MOFs) or porous coordination polymers (PCPs) have been attracting considerable interest because of the rich variety of structural designs as well as their diverse chemical/physical properties.[1–3] Even though MOFs themselves exhibit diverse properties such as gas sorption, molecular recognition/separation and catalytic activity, hybridization of MOFs with other materials including metals and metal oxides offers the opportunity to enhance such properties or enable new behaviors.[4–7] For example, high selectivity[1–3] and condensation behavior[8,9] for stored molecules in MOF pores have been reported. Incorporation of such unique features into inorganic catalysts may enhance their catalytic activity. The major methods of preparing MOF/inorganic composites involve either using MOFs as templates to create inorganic nanoparticles in their pores[10–12] or covering pre-synthesized inorganic particles with MOFs.[13–15] In the former case, size-regulated nanoparticles/nanoclusters can be generated within the MOF cavities. In the latter case, core/shell structures, in which the inorganic particle is the core and the MOF is the shell can be formed. Although such core/shell composites have been reported,[13–15] fine control of the MOF shell shape and thickness on the nanoscale still remains an important issue to address, in contrast to the well-established methodologies for tuning the size of metal/metal oxide nanoparticles. On flat substrate surfaces, MOFs can be prepared in a finely-controlled thin film state by a solution-based step-by-step methodology.[16–21] A major advantage of this approach is that it provides excellent tuning of the film thickness on the nanoscale by varying the number of deposition cycles. We have reported the first successful application of this technique to lithium cobalt oxide (LCO) particle surfaces for which deposition and step-by-step modification of Prussian blue framework nanolayers were achieved.[22]

LCO is one of the most well-known compounds utilized as a cathode active material for lithium ion batteries.[23–26] Recently, the catalytic properties of LCO for oxygen evolution and oxygen reduction reactions have been also actively investigated.[27–29] The catalytic activity was improved by fine tuning the electrochemical potential of LCO *via* extraction of lithium ions.[27] Iron(II) oxalate dihydrate, $[Fe(ox)(H_2O)_2]$ is a dense MOF because of the small size of the multidentate ligand, oxalate ion.[30–34] Such a small size of the building unit offers an opportunity of fine tuning the MOF shell thickness. Although thin film creation of Fe(ox) by a solution-based step-by-step approach has been attempted, formation of the Fe(ox) framework on the solid substrate has remained

[a] *Department of Materials Science, Graduate School of Engineering, Osaka Prefecture University, Sakai, Osaka 599-8570, Japan. E-mail: r-makiura@mtr.osakafu-u.ac.jp*
[b] *Department of Applied Chemistry, Graduate School of Engineering, Osaka Prefecture University, Sakai, Osaka 599-8531, Japan*

† Electronic supplementary information (ESI) available. See DOI: 10.1039/c7ce00552k

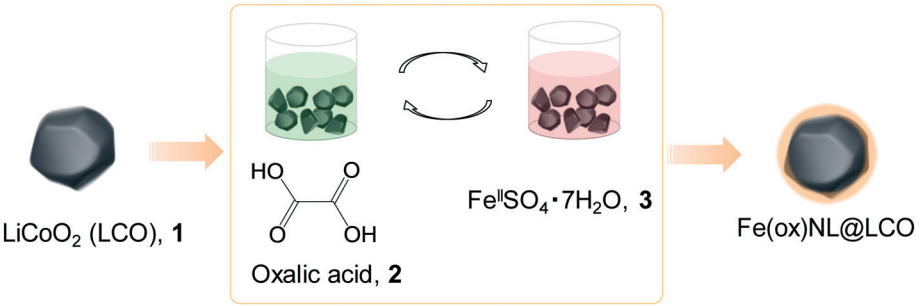

Fig. 1 Schematic illustration of the surface coating of $LiCoO_2$ with iron(II) oxalate. $LiCoO_2$ (LCO) particles, **1**, are alternately immersed into ethanol solutions of oxalic acid, **2**, and aqueous solutions of $FeSO_4{\cdot}7H_2O$, **3**, including intermediate solvent (ethanol or water as appropriate) rinsing and room temperature drying steps. This sequential step-by-step procedure results in the generation of an iron(II) oxalate (Fe(ox))-coated LCO particle surface (Fe(ox)NL@LCO) of controllable amount.

unclear.[35] In addition, there have been no reports employing Fe(ox) as a MOF shell to create core/shell hybrid materials. Here, we demonstrate how the solution-based step-by-step modification protocol can be successfully employed to coat LCO particle surfaces with the dense framework Fe(ox) material to afford LCO/Fe(ox) core/shell hybrid composites.

Experimental

Sequential surface modification of $LiCoO_2$ with iron(II) oxalate (Fe(ox)NL@LCO)

The following procedures, labelled (i) and (ii), were conducted sequentially. (i) 2 g of $LiCoO_2$ (LCO, Nippon Chemical Industrial Co., Ltd.), **1**, was dispersed into 50 mL of either 5 or 10 mM oxalic acid (Kanto Chemical Co., Inc), **2**, solution in ethanol. The solution was kept stirring for 10 min. LCO dispersed in the oxalic acid solution was filtered, washed with ethanol, and dried in air. (ii) The collected LCO particles with attached oxalic acid were added into 50 mL of either 5 or 10 mM $FeSO_4{\cdot}7H_2O$ (Kanto Chemical Co., Inc.), **3**, aqueous solution. The solution was kept stirring for 10 min and filtered. In order to remove excess **3**, after collection, the LCO particles were washed with purified water under stirring and filtered. The set of procedures (i) and (ii) is counted as a single cycle and we repeated it up to five times. The LCO particles coated with iron(II) oxalate nanolayers (Fe(ox)NL@LCO) were dried at 80 °C under vacuum for three hours. We confirmed by TG-DTA measurements that Fe(ox) remains stable up to at least 140 °C (Fig. S1†).

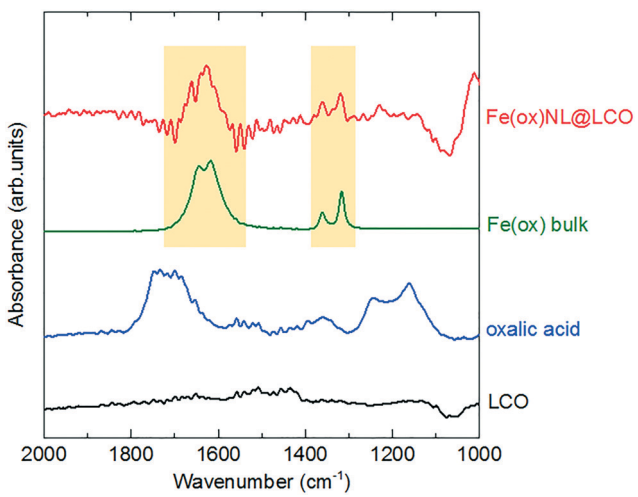

Fig. 2 Infrared (IR) absorption spectra of Fe(ox)NL@LCO. IR spectrum of the LCO particles following three successive Fe(ox) nanolayer deposition cycles – Fe(ox)NL3c@LCO (red solid line). IR spectra of bulk Fe(ox) powder (green line), oxalic acid (blue line) and uncoated LCO (black line) are also shown for comparison. Observation of the absorption bands in the spectral regions near 1350 and 1600 cm^{-1} in Fe(ox)NL3c@LCO confirms the formation of Fe(ox) frameworks on the LCO surface.

Infrared (IR) absorption spectroscopy

The IR absorption spectra of the Fe(ox)NL@LCO samples were collected using a Jasco FT-IR/620 Fourier transform infrared spectrometer at room temperature under vacuum conditions. All spectra were recorded with a 4 cm^{-1} resolution.

Scanning electron microscopy (SEM)

The morphology of the Fe(ox)NL@LCO samples was examined by scanning electron microscopy (SEM, JSM-6610A, JEOL) equipped with an energy-dispersive X-ray spectroscopy system (EDX, JED-2300, JEOL). Elemental analysis was conducted by EDX. Four different images with a 200-power magnification (more than 1000 LCO particles are included) of each sample were used for creating the EDX spectra. Fe and Co contents were evaluated by averaging the numbers derived from the spectra.

Impedance spectroscopy

Electrical conductivity data of the Fe(ox)NL@LCO samples were collected by AC impedance measurements using a Solartron 1260 impedance analyzer in the frequency range 10 Hz to 1 MHz. The measurements were conducted with pelletized samples of 10 mm in diameter and about 0.3 mm in thickness. The pellet samples were prepared by applying a uniaxial pressure of 370 MPa for five minutes at room temperature and stainless steel plates were used as current collectors.

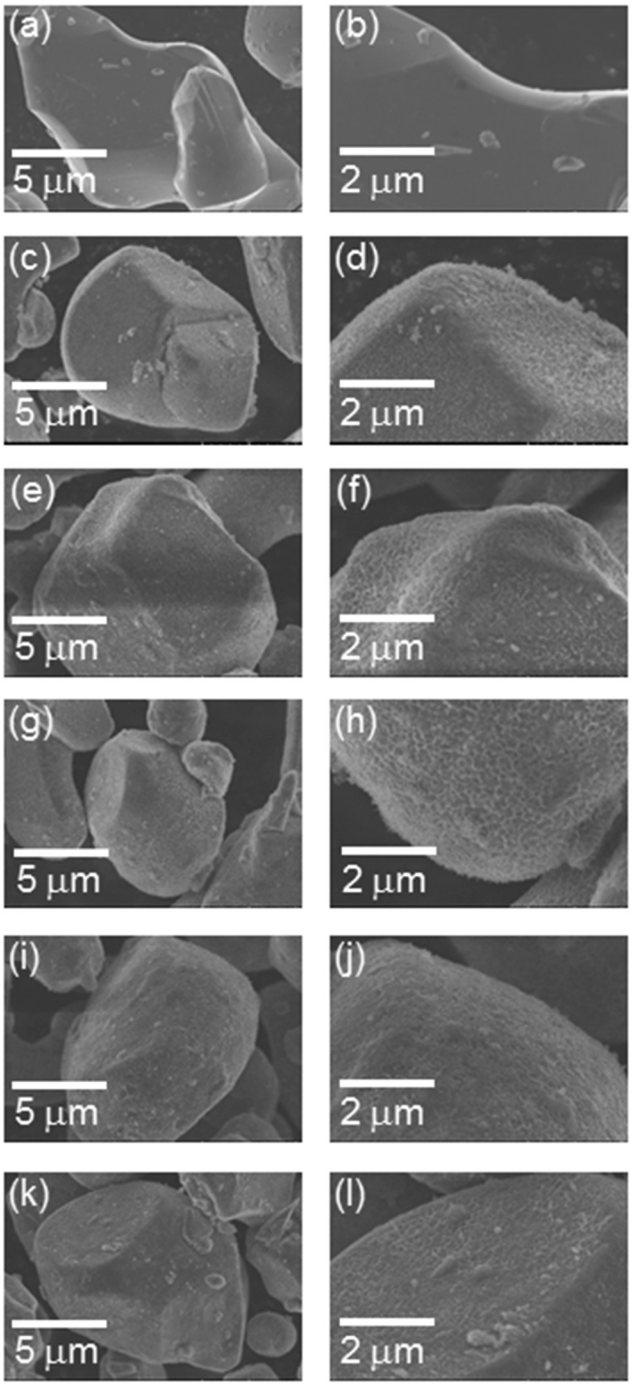

Fig. 3 Surface morphology of Fe(ox)NL@LCO. (a)–(l) Scanning electron microscopy (SEM) images of the uncoated LCO particles (a)/(b) and the LCO particles following one, two, there, four and five successive Fe(ox) nanolayer deposition cycles (1c, 2c, 3c, 4c and 5c, respectively) – Fe(ox)NL1c@LCO (c)/(d), Fe(ox)NL2c@LCO (e)/(f), Fe(ox)NL3c@LCO (g)/(h), Fe(ox)NL4c@LCO (i)/(j) and PBNL5c@LCO (k)/(l).

Results and discussion

Successive surface modification and characterization

The surface modification procedure involves the alternate immersion of $LiCoO_2$ (LCO), **1**, particles into ethanolic solutions of oxalic acid, **2**, and aqueous solutions of $FeSO_4{\cdot}7H_2O$, **3** (Fig. 1). This sequential step-by-step procedure, which also includes intermediate solvent (ethanol or water, as appropriate) immersion and room temperature drying steps results in the generation of iron(II) oxalate nanolayers (Fe(ox)NL) on the LCO particle surface (Fe(ox)NL@LCO).

The formation of Fe(ox) on the LCO surface was monitored by infrared (IR) absorption spectroscopy (Fig. 2). Oxalic acid shows a strong absorption around 1700 cm^{-1} attributed to the C═O stretching mode. On the other hand, the COO stretching modes (at ~1350 and ~1600 cm^{-1}) become active when Fe(ox) forms[30] and the C═O stretching mode disappears. Clear observation of bands at around 1350 and 1600 cm^{-1} in Fe(ox)NL@LCO provides strong evidence for the formation of Fe(ox) on the LCO particle surface. We also collected powder X-ray diffraction (PXRD) data of the Fe(ox)NL@LCO samples (Fig. S2†). However, the small content of Fe(ox) in the sample relative to that of LCO in the core did not allow the observation of any peaks attributable to Fe(ox) – all Bragg reflections can be assigned to LCO and structural characterization of the Fe(ox) nanolayers is therefore precluded. We note that in earlier synchrotron XRD work on Fe(ox) nanolayers grown on a flat sapphire substrate,[35] a chain structure of deposited Fe(ox) was proposed analogous to that of the bulk material.[36,37] As the sapphire-deposited nanolayers were fabricated by a comparable technique to that employed in the present work of alternate immersion of the substrate into oxalic acid and iron sulfate solutions, we consider that the Fe(ox) nanolayers formed on the LCO particles might also adopt the same chain structure.

Surface morphology

The modification of the surface morphology of the LCO particles before and after Fe(ox)NL deposition was examined by scanning electron microscopy (SEM). Fig. 3 shows images of the LCO surface following one, two, three, four and five successive Fe(ox) nanolayer coating cycles (1c, 2c, 3c, 4c and 5c, respectively) together with that of the uncoated LCO particles. The morphology is markedly different from that of the LCO surface in the absence of any Fe(ox) coating treatment – the surface of uncoated LCO particles is smooth (Fig. 3a and b) and contrasts with the roughness characterizing the Fe(ox)NL@LCO surfaces (Fig. 3c–l). We note that the roughness seen in the Fe(ox)NL@LCO surfaces tends to diminish with increasing number of coating cycles.

Fe(ox) growth on LCO surface

The elemental mapping images obtained by energy-dispersive X-ray spectroscopy (EDX) for Fe(ox)NL3c@LCO are shown in Fig. 4a–c. Fe atoms from the coating material, Fe(ox), are homogeneously distributed over the entire surface area in the same way as Co atoms from the LCO particles, confirming that Fe(ox)NL has uniformly coated the LCO surface.

The step-by-step Fe(ox) framework growth was also monitored by EDX analysis. The evolution of Fe and Co content

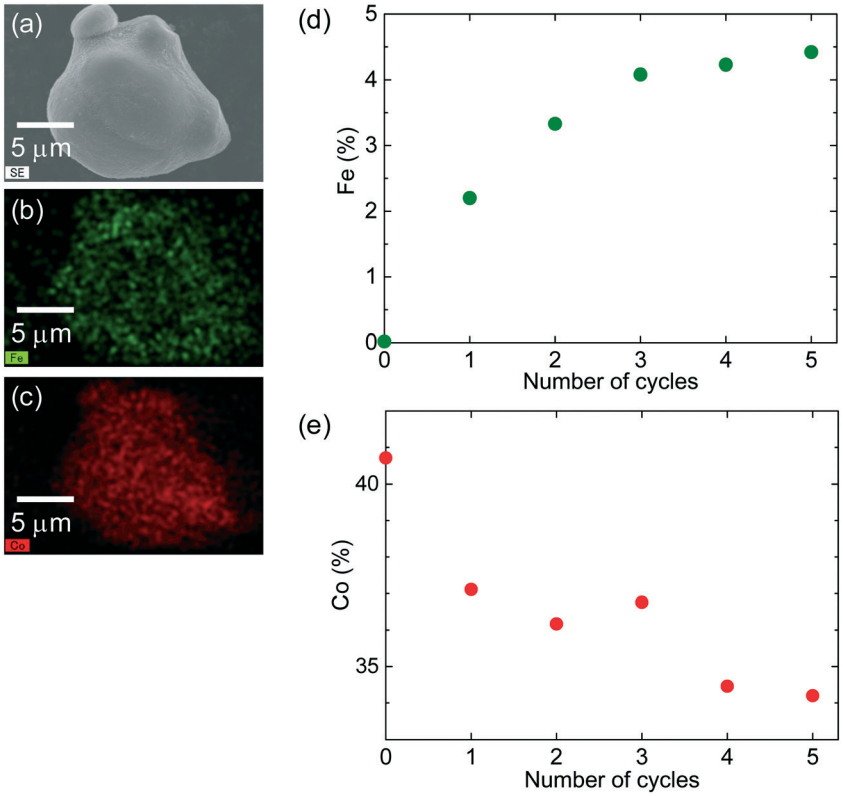

Fig. 4 Elemental analysis of Fe(ox)NL@LCO and Fe(ox) growth on LCO surfaces followed by energy-dispersive X-ray spectroscopy (EDX). (a)–(c) Elemental mapping obtained by EDX analysis for Fe(ox)NL4c@LCO. Mapping elements are Fe (b) from Fe(ox) and Co (c) from LCO. The corresponding SEM image of the Fe(ox)NL4c@LCO particle is shown in (a). (d) and (e) Plots of Fe (d) and Co (e) content (%) *versus* number of Fe(ox) growth cycles. Estimated errors are smaller than the size of the symbols.

was monitored as a function of the number of coating cycles (Fig. 4d and e). The observed growth of Fe is accompanied by a decrease in Co content and provides evidence for the successful Fe(ox) growth on the LCO surface in a sequential manner. However, the increase in Fe content with the number of modification cycles is not linear and shows a tendency for saturation after three cycles. This contrasts with the case of the Prussian blue nanolayer coating on LCO particle surfaces where it was established that the number of nanolayers increased monotonically with the number of modification cycles.[22] In the present case, the observed behavior implies that the deposited Fe(ox) frameworks do not grow vertically on the particle surface. Instead, they appear to grow parallel or at some angle to the particle surface. Therefore, once the LCO surface is well covered by Fe(ox) and all connective parts are used up, further modification procedures do not lead to any additional surface growth of Fe(ox).

Electrical properties

In order to examine the influence of the Fe(ox)NL surface coating on the LCO electrical properties, the resistivity of the Fe(ox)NL@LCO samples was measured by an impedance spectroscopy technique. Fig. 5a shows the complex impedance curves obtained from the pellet-shaped samples of LCO particles after one, two, three, four and five cycles of Fe(ox) NL deposition treatment together with that of the uncoated LCO for comparison. The details of the analysis procedure of the impedance curves are shown in Fig. S3.† The total resistance increases with increasing number of coating cycles. The impedance spectra in the Nyquist representation for all the samples comprise one semicircle with each spectrum containing two resistive components: the bulk resistance inside the LCO particles (R_0) and the grain boundary resistance (R_1), as shown in Fig. 5b. After taking into account the pellet area and thickness, the evolution of the resistivity with the number of Fe(ox)NL coating cycles is shown in Fig. 5c. R_0 shows no change as the LCO internal resistance is not affected by the surface coating. However, R_1 changes as the number of Fe(ox)NL coating cycles increases – it increases sharply for the first two cycles, but then saturates and decreases after the third deposition cycle remaining roughly unchanged. As Fe(ox) is an electrical insulator, its deposition on the LCO surface initially leads to an increase in R_1, as also observed in the Prussian-blue-nanolayer-coated LCO samples.[22] However, unlike insulating Prussian blue frameworks, Fe(ox) is a good proton conductor[36,37] and shows a robust ion-intercalation capability.[38] This behavior together with the evolution of the Fe content with increasing number of deposition cycles established by the EDX analysis can be used to rationalize the non-monotonic changes in R_1. Initially, a small number of modification cycles (1–3 cycles) leads to the

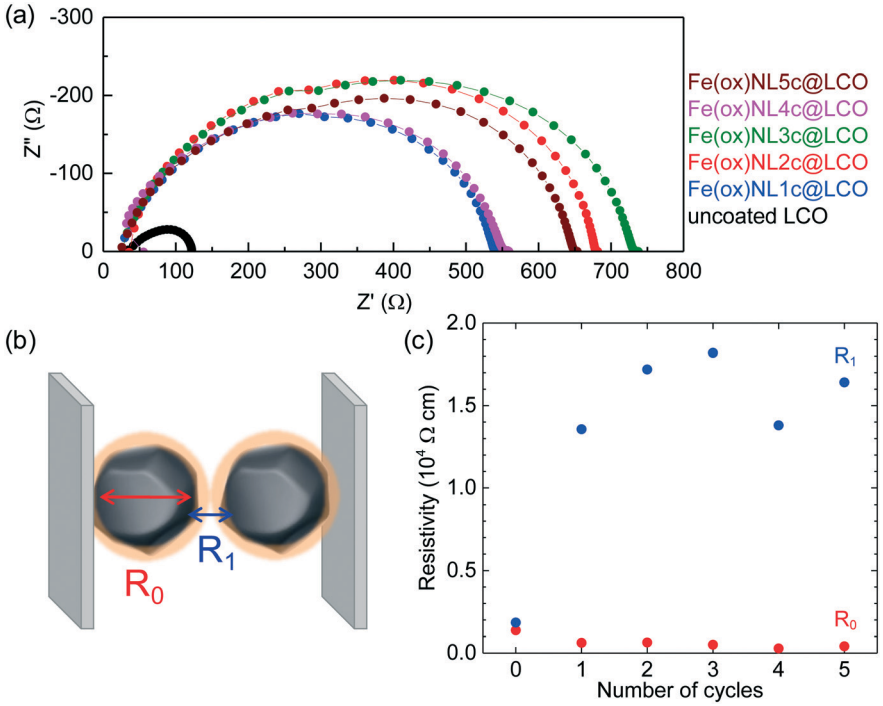

Fig. 5 Complex impedance curves for Fe(ox)NL@LCO. (a) Impedance spectra in the Nyquist representation obtained from pellet-shaped uncoated LCO (black), Fe(ox)NL1c@LCO (blue), Fe(ox)NL2c@LCO (red), Fe(ox)NL3c@LCO (green), Fe(ox)NL4c@LCO (pink), and Fe(ox)NL5c@LCO (brown). (b) Schematic image of the resistive components: bulk resistance inside the LCO particles (R_0) and grain boundary resistance (R_1). We consider that the contact resistance between the LCO particles and the electrode is included in R_1 or appears in a lower frequency region. (c) Evolution of R_0 (red circles) and R_1 (blue circles) with the number of Fe(ox)NL coating cycles.

creation of island-like grown Fe(ox) domains on the LCO surfaces and is accompanied by an increase in R_1. Additional deposition cycles (4–5 cycles) lead to growth and coalescence of the domains to form continuous Fe(ox) frameworks covering the LCO surfaces, thereby creating proton or lithium ion conduction paths, which lead to a reduction in R_1.

Conclusion

The results presented here show that the solution-based step-by-step modification of $LiCoO_2$ (LCO) particle surfaces with iron(II) oxalate (Fe(ox)) leads to the creation of a hybrid core/shell-type material. IR spectroscopy revealed the formation of Fe(ox) frameworks on the LCO surface upon its alternate immersion into each of the starting compound solutions, oxalic acid and $FeSO_4{\cdot}7H_2O$. The increasingly reduced roughness of the surface morphology of the coated particles and the accompanying saturation of the Fe content as the number of modification cycles increases imply that the Fe(ox) framework grows laterally on the particle surface and the growth tends to be complete after only a few deposition cycles. As a result, the continuous increase of the electrical resistivity of Fe(ox)-coated LCO is suppressed. This is of importance in preventing undesired electrochemical potential changes, which can affect the catalytic activity. We consider that the coating strategy presented here is sufficiently versatile to open a new direction towards the facile modification of inorganic catalysts with nanolayers of stable framework compounds. Fabrication of core/shell catalyst/MOF composites can contribute to the improvement of the structural stability of the core objects as well as to the enhancement of their reaction activity arising from the MOFs' highly selective and/or condensation features to reactants.

Acknowledgements

We acknowledge financial support from the Japan Science and Technology Agency (JST) on "Advanced Low Carbon Technology Research and Development Program (ALCA)" and "Precursory Research for Embryonic Science and Technology (PRESTO)" for a project of "Molecular technology and creation of new functions (JPMJPR12K8)", the Japan Society for the Promotion of Science (JSPS) on "Grants-in-Aid for Scientific Research, KAKENHI (16H05968, 16K13610)" and the Foundation for The Promotion of Ion Engineering. We thank Dr. M. Menelaou for TG-DTA measurements.

References

1 S. Kitagawa, R. Kitaura and S. Noro, Functional porous coordination polymers, *Angew. Chem., Int. Ed.*, 2004, **43**, 2334–2375.
2 H.-C. Zhou, J. R. Long and O. M. Yaghi, Introduction to metal–organic frameworks, *Chem. Rev.*, 2012, **112**, 673–674.
3 G. Ferey, Hybrid porous solids: past, present, future, *Chem. Soc. Rev.*, 2008, **37**, 191–214.

4 Q.-L. Zhu and Q. Xu, Metal–organic framework composites, *Chem. Soc. Rev.*, 2014, **43**, 5468–5512.
5 S. Li and F. Huo, Metal–organic framework composites: from fundamentals to applications, *Nanoscale*, 2015, **7**, 7482–7501.
6 J.-K. Sun and Q. Xu, Functional materials derived from open framework templates/precursors: synthesis and applications, *Energy Environ. Sci.*, 2014, **7**, 2071–2100.
7 P. Falcaro, R. Ricco, C. M. Doherty, K. Liang, A. J. Hill and M. J. Styles, MOF positioning technology and device fabrication, *Chem. Soc. Rev.*, 2014, **43**, 5513–5560.
8 J. Canivet, A. Fateeva, Y. Guo, B. Coasne and D. Farrusseng, Water adsorption in MOFs: fundamentals and applications, *Chem. Soc. Rev.*, 2014, **43**, 5594–5617.
9 J. Landers, G. Y. Gor and A. V. Neimark, Density functional theory methods for characterization of porous materials, *Colloids Surf., A*, 2013, **437**, 3–32.
10 S. Hermes, M. K. Schröter, R. Schmid, L. Khodeir, M. Muhler, A. Tissler, R. W. Fischer and R. A. Fischer, Metal@MOF: loading of highly porous coordination polymers host lattices by metal organic chemical vapor deposition, *Angew. Chem., Int. Ed.*, 2005, **44**, 6237–6241.
11 S. Turner, O. I. Lebedev, F. Schröder, D. Esken, R. A. Fischer and G. V. Tendeloo, Direct imaging of loaded metal–organic framework materials (metal@MOF-5), *Chem. Mater.*, 2008, **20**, 5622–5627.
12 G. Lu, S. Li, Z. Guo, O. K. Farha, B. G. Hauser, X. Qi, Y. Wang, X. Wang, S. Han, X. Liu, J. S. Duchene, H. Zhang, Q. Zhang, X. Chen, J. Ma, S. C. J. Loo, W. D. Wei, Y. Yang, J. T. Hupp and F. Huo, Imparting functionality to a metal–organic framework material by controlled nanoparticle encapsulation, *Nat. Chem.*, 2012, **4**, 310–316.
13 T. Zhang, X. Zhang, X. Yan, L. Kong, G. Zhang, H. Liu, J. Qiu and K. L. Yeung, Synthesis of Fe_3O_4@ZIF-8 magnetic core–shell microspheres and their potential application in a capillary microreactor, *Chem. Eng. J.*, 2013, **228**, 398–404.
14 L. D. O'Neill, H. Zhang and D. Bradshaw, Macro-/microporous MOF composite beads, *J. Mater. Chem.*, 2010, **20**, 5720–5726.
15 P. Falcaro, F. Normandin, M. Takahashi, P. Scopece, H. Amenitsch, S. Costacurta, C. M. Doherty, J. S. Laird, M. D. H. Lay, F. Lisi, A. J. Hill and D. Buso, Dynamic control of MOF-5 crystal positioning using a magnetic field, *Adv. Mater.*, 2011, **23**, 3901–3906.
16 O. Shekhah, H. Wang, S. Kowarik, F. Schreiber, M. Paulus, M. Tolan, C. Sternemann, F. Evers, D. Zacher, R. A. Fischer and C. Wöll, Step-by-step route for the synthesis of metal–organic frameworks, *J. Am. Chem. Soc.*, 2007, **129**, 15118–15119.
17 R. Makiura, S. Motoyama, Y. Umemura, H. Yamanaka, O. Sakata and H. Kitagawa, Surface nano-architecture of a metal–organic framework, *Nat. Mater.*, 2010, **9**, 565–571.
18 R. Makiura, K. Tsuchiyama and O. Sakata, Self-assembly of highly crystalline two-dimensional MOF sheets on liquid surfaces, *CrystEngComm*, 2011, **13**, 5538–5541.
19 R. Makiura and O. Konovalov, Bottom-up assembly of ultrathin sub-micron size metal–organic framework sheets, *Dalton Trans.*, 2013, **42**, 15931–15936.
20 R. Makiura and O. Konovalov, Interfacial growth of large-area single-layer metal–organic framework nanosheets, *Sci. Rep.*, 2013, **3**, 2506–2513.
21 R. Makiura, R. Usui, Y. Sakai, A. Nomoto, A. Ogawa, O. Sakata and A. Fujiwara, Towards rational modulation of in-plane molecular arrangements in metal–organic framework nanosheets, *ChemPlusChem*, 2014, **79**, 1352–1360.
22 R. Makiura, S. Teragawa, K. Tsuchiyama, A. Hayashi, K. Tadanaga and M. Tatsumisago, Liquid-phase step-by-step growth of an iron cyanide coordination framework on $LiCoO_2$ particle surfaces, *Dalton Trans.*, 2015, **44**, 15279–15285.
23 J.-M. Tarascon and M. Armand, Issues and challenges facing rechargeable lithium batteries, *Nature*, 2001, **414**, 359–367.
24 F. Croce, G. B. Appetecchi, L. Persi and B. Scrosati, Nanocomposite polymer electrolytes for lithium batteries, *Nature*, 1998, **394**, 456–458.
25 T. Minami, A. Hayashi and M. Tatsumisago, Recent progress of glass and glass-ceramics as solid electrolytes for lithium secondary batteries, *Solid State Ionics*, 2006, **177**, 2715–2720.
26 J. N. Reimers and J. R. Dahn, Electrochemical and in situ x-ray diffraction studies of lithium intercalation in Li_xCoO_2, *J. Electrochem. Soc.*, 1992, **139**, 2091–2097.
27 G. P. Gardner, Y. B. Go, D. M. Robinson, P. F. Smith, J. Hadermann, A. Abakumov, M. Greenblatt and G. C. Dismukes, Structural requirements in lithium cobalt oxides for the catalytic oxidation of water, *Angew. Chem., Int. Ed.*, 2012, **51**, 1616–1619.
28 Z. Lu, H. Wang, D. Kong, K. Yan, P.-C. Hsu, G. Zheng, H. Yao, Z. Liang, X. Sun and Y. Cui, Electrochemical tuning of layered lithium transition metal oxides for improvement of oxygen evolution reaction, *Nat. Commun.*, 2014, **5**, 4345.
29 T. Maiyalagan, K. A. Jarvis, S. Therese, P. J. Ferreira and A. Manthiram, Spinel-type lithium cobalt oxide as a bifunctional electrocatalyst for the oxygen evolution and oxygen reduction reactions, *Nat. Commun.*, 2014, **5**, 3949.
30 K. S. Rane, A. K. Nikumbh and A. J. Mukhedkar, Thermal decomposition of ferrous oxalate dihydrate studied by direct current electrical conductivity measurements, *J. Mater. Sci.*, 1981, **16**, 2387–2397.
31 Y. Feng, T. Hu, Z. Pu, M. Wu and J. Mi, Non-isothermal decomposition kinetics of $FeC_2O_4{\cdot}2H_2O$ prepared by solid–state method aiming at the formation of Fe_2O_3, *J. Therm. Anal. Calorim.*, 2015, **122**, 947–953.
32 S. Decurtins, R. Pellaux, G. Antorrena and F. Palacio, Multifunctional coordination compounds: design and properties, *Coord. Chem. Rev.*, 1999, **190–192**, 841–854.
33 M. B. Hursthouse, M. E. Light and D. J. Price, One-dimensional magnetism in anhydrous iron and cobalt ternary oxalates with rare trigonal-prismatic metal coordination environment, *Angew. Chem., Int. Ed.*, 2004, **43**, 472–475.
34 C. Train, M. Gruselle and M. Verdaguer, The fruitful introduction of chirality and control of absolute configurations in molecular magnets, *Chem. Soc. Rev.*, 2011, **40**, 3297–3312.

35 R. Haruki, O. Sakata, T. Yamada, K. Kanaizuka, R. Makiura, Y. Akita, M. Yoshimoto and H. Kitagawa, Structural evaluation of an iron oxalate complex layer grown on an ultra-smooth sapphire (0001) surface by a wet method, *Trans. Mater. Res. Soc. Jpn.*, 2008, **33**, 629–631.
36 T. Yamada, M. Sadakiyo and H. Kitagawa, High proton conductivity of one-dimensional ferrous oxalate dihydrate, *J. Am. Chem. Soc.*, 2009, **131**, 3144–3145.
37 S. Tominaka and A. K. Cheetham, Intrinsic and extrinsic proton conductivity in metal–organic frameworks, *RSC Adv.*, 2014, **4**, 54382–54387.
38 X. Wang, R. Kurono, S. Nishimura, M. Okubo and A. Yamada, Iron-oxalato framework with one-dimensional open channels for electrochemical sodium–ion intercalation, *Chem. – Eur. J.*, 2015, **21**, 1096–1101.